PAPER • OPEN ACCESS

Investigation of a low frequency coherent mode in Wendelstein 7-X with island divertor

OPEN ACCESS
IOP Publishing | International Atomic Energy Agency
Nuclear Fusion
Nucl. Fusion **63** (2023) 126050 (13pp)
https://doi.org/10.1088/1741-4326/ad0415

Investigation of a low frequency coherent mode in Wendelstein 7-X with island divertor

H.M. Xiang[1,2,3,*], A. Krämer-Flecken[3], X. Han[5,7], T. Windisch[4], G. Weir[4], K. Rahbarnia[4], J. Schilling[4], H. Thomsen[4], S.vaz Mendes[4], A. Knieps[3], M. Vécsei[6], M. Otte[4], S. Zoletnik[6], G. Anda[6], D. Dunai[6], D. Zhang[4], P. Kornejew[4], J. Huang[5], T. Zhang[5], X.D. Lin[1,2], X. Gao[1,2,5], Y. Liang[3,5] and the W7-X team[a]

[1] College of Physics and Optoelectronic Engineering, Shenzhen University, Shenzhen 518060, China
[2] Advanced Energy Research Center, Shenzhen University, Shenzhen 518060, China
[3] Forschungszentrum Jülich GmbH, Institute für Energie-und Klimaforschung—Plasmaphysik, Partner of the Trilateral euregio Cluster (TEC), 52425 Jülich, Germany
[4] Max-Planck-Institut für Plasmaphysik, 17491 Greifswald, Germany
[5] Institute of Plasma Physics, Chinese Academy of Sciences, 230031 Hefei, Anhui, China
[6] Centre for Energy Research, H-1525 Budapest, Hungary
[7] University of Wisconsin, Madison, WI 53705, United States of America

E-mail: h.xiang@fz-juelich.de

Received 29 June 2023, revised 11 August 2023
Accepted for publication 17 October 2023
Published 31 October 2023

Abstract

During the island divertor operation of W7-X, especially in standard magnetic configuration (with 5/5 island chain in the scrape-off-layer (SOL)), quasi-periodic electromagnetic oscillation is observed. It appears in the frequency range of 1 kHz–2 kHz, therefore it is called the low frequency mode (LFM) within this paper. It is observed by multiple diagnostics, amongst them, a poloidal correlation reflectometer allowing radial localization of the LFM. The LFM is localized in the SOL and shows an obvious modulation effect on the plasma perpendicular velocity ($V_{\perp}$). Furthermore, broadband turbulence is observed in the fluctuation spectra of the electron density and the magnetic field and the perpendicular correlation length of turbulence eddies are modulated. The calculation of the poloidal flow velocity and its oscillation allows us to study the effect of the LFM on the flow. Cross correlation analysis shows that the perpendicular flow oscillation and the turbulence modulation are closely correlated. The application of external control coils to adjust the island size and position result in a strong modification of the magnetic topology at the plasma edge which affects the appearance, amplitude and frequency of the LFM. Bi-coherence analysis indicates that nonlinear interactions among turbulence components is a possible mechanism for the generation of the LFM.

[a] See Sunn Pedersen *et al* 2022 (https://doi.org/10.1088/1741-4326/ac2cf5) for the W7-X Team.
[*] Author to whom any correspondence should be addressed.

Keywords: turbulence modulation, velocity oscillation, low frequency mode

(Some figures may appear in colour only in the online journal)

1. Introduction

To achieve high energy and particle confinement in magnetically confined fusion plasmas, the role of plasma turbulence and its impact on the radial transport has to be investigated. The plasma turbulence with its intrinsic quality of complex dynamics [1] has been recognized as a major player for the underlying anomalous transport [2–9]. In this sense, a better understanding of the turbulence and any mechanism influencing and limiting its development is valuable and should be thoroughly investigated. Past experiments have been performed to measure the local plasma parameters (such as radial electric field E_r, electron temperature T_e, electron density n_e and pressure gradient) with high spatio-temporal resolution, trying to find the key element in determining the relation between turbulence and gradients. It has been found that the turbulence amplitude and the spatial correlation properties, such as the radial correlation length of turbulence eddies, could be affected by the presence of a strong velocity shear layer, resulting in the reduction of transport [10] and even suppression of turbulence related to the formation of transport barriers [11, 12]. In addition to the effects of mean E_r, two well known oscillatory sheared flows are known as zonal flows and geodesic acoustic modes (GAMs) [13–15]. They are radial localized $E \times B$ plasma flows generated by non-linear interactions with plasma turbulence and contribute to the regulation of plasma turbulence via a shearing effect, reducing turbulent cross-field transport.

Also, magneto-hydrodynamic (MHD) modes can strongly influence the turbulence and plasma flow thereafter modulate its induced transport. Tearing modes modulate turbulence and the plasma flow in the plasma core, as reported in tokamaks [16–21]. Furthermore, there are investigations of turbulence coherent structures modulated by the kink instability and micro-turbulence modulated by the low-frequency mode (LFM) in the H-mode pedestal region [22, 23]. Turbulence and plasma flows are known to be modulated by MHD modes in different confinement regimes and regions indicating common features of cross-scale interaction, which is of significant importance for further study in order to find possibilities to control turbulence and induced transport.

The stellarator, with its intrinsic advantages of steady state operation and absence of disruptions, has attracted attention in magnetic confinement fusion research [24, 25]. W7-X [26–28] is an advanced stellarator where the neoclassical transport is optimized and the radial transport is mainly driven by plasma turbulence. The intrinsic forming of an island divertor in the scrape-off-layer (SOL) result in longer connection lengths (in the order of a few hundred meters) and therefore a longer power decay length, which is beneficial for particle and power exhaust [29]. This is of importance, especially, when aiming for long pulse operation. Various factors influence the turbulence such as (i) the 3D structure of the SOL, (ii) the gradients and (iii) the radial electric field shear, which all together make the cross field transport more complicated. The investigation [30] shows that the magnetic topology plays an essential role for turbulent transport. Moreover, filament structures which are known to influence SOL transport are observed in W7-X [31] and show a difference in the intermittency when compared with tokamaks (e.g. AUG [32]). Since SOL dynamics and transport are fundamental for the assessment of the divertor performance, the understanding of different turbulence components influencing the SOL properties is of importance. During the experiments with island divertor configurations, a coherent oscillation in the frequency range of 1 kHz–2 kHz (LFM) is observed within a broad range of plasma parameters [33], especially in the standard magnetic configuration. The investigation [33] describes the mode structures and their correlations with different plasma parameters, e.g., heating power and density. However, further investigations on the localization of the 1 kHz–2 kHz oscillation and its influence on the key elements related to cross-field transport and the possible mechanism for the generation of LFM are still unknown. These issues will be investigated in more detail in this paper. The paper is organized as follows. The experimental set up and the diagnostics will be introduced in section 2. The experimental observation of the LFM will be presented in section 3, including its characterization. Furthermore, the observed turbulence modulation and velocity oscillations, as well as the relationship between these two phenomena are presented in this section. Moreover, the dynamics of LFM observed during the experiments with control coils is investigated. As a last point, a possible mechanism for the generation of LFM is proposed. Finally, a summary will be given in section 4.

2. Experimental set up on W7-X

W7-X is a stellarator with a five-fold toroidal symmetry and with major radius $R = 5.5\,\mathrm{m}$ and minor radius $a = 0.5\,\mathrm{m}$. It is equipped with 50 non-planar and 20 planar superconducting coils offering a large variety of magnetic configurations. The experimental results presented in this work are performed for plasma in a standard magnetic configuration (EJM), where the majority of the systematic investigations of island divertor experiments are conduced in OP1.2b. It is characterized by an edge rotational transform iota (n/m, where n and m denote the toroidal and poloidal mode numbers, respectively) equal to one at the last closed flux surface (LCFS) and a large $5/5$ islands chain dominates the SOL. The island chain intersects with divertor plates, resulting in regions with open field lines and a remnant island varying in shape and size. The divertor control coils with two coils per

module, are available to adjust the divertor islands in position and shape. Applying positive currents in both coils increases the size of the island and negative currents will decrease its size [34, 35]. In addition, the inverted currents are capable of sweeping the island position, poloidally. Besides those effects, the island size is subject to changes of the toroidal plasma current [35].

A poloidal correlation reflectometer (PCR) [36–38] in W7-X intends to measure the spatio-temporal evolution of density fluctuations and the perpendicular velocity at the interface between edge and core plasmas [39–43]. It is installed slightly below the equatorial plane in a bean-shaped plasma cross-section at a toroidal location of $\phi = 71.1°$, as seen in figure 1. Figure 1(a) shows the Poincaré map at the cross-section of PCR. It is seen that the line of sight (LoS) of all antennae intersects the magnetic island. The Poincaré map is obtained from the field line tracer [44], which calculates the magnetic field using the Biot–Savart law with the input of coil current. The calculation here considers the main coils for vacuum magnetic field only. Figure 1(a) shows the arrangement of antennae array. The antenna array consists of one launcher (labeled A) surrounded by four receivers (B, C, D, E), where the receivers B and C share the same poloidal cross-section as A, and the receivers D and E are mounted poloidally in the adjacent cross-section. The reflected wave of each antenna is measured by a quadrature detector (I/Q signal) and sampled with a frequency of 4 MHz. The arrangement of antenna array yields six different antennae combinations clockwise, e.g. BD, EC, DE, BE, EC, BC. Except the different poloidal localized measurements from each single antenna, the cross correlation between antennae combinations offers more information on the poloidal turbulence propagation. This analysis will be shown in section 3.

The system operates in O-mode polarization in a frequency hopping mode from 22 GHz to 40 GHz, corresponding to a cutoff n_e of $0.6 \times 10^{19}\mathrm{m}^{-3}$–$2 \times 10^{19}\mathrm{m}^{-3}$. Usually, the frequency follows a staircase-like shape with frequency steps of 0.5 GHz and step duration of 20 ms. The availability of density profiles is an important factor for the radial localization of PCR measurements. Inside the LCFS Thomson scattering provides density profiles which can be mapped with the help of the 3D-MHD-equilibrium code VMEC [45] to the position of the PCR. In addition, the Alkaline Beam diagnostic (ABES) [46] can measure density profiles as well. It is located at the equatorial plane of the same port as PCR, at a toroidal angle of $\phi = 72°$. The achieved density profiles can be mapped to the position of the PCR. For plasmas with higher electron density, the measurement of PCR is mainly located in the SOL while at moderate electron density, plasma edge and gradient region are accessible.

In general, the turbulence structures are strongly elongated along the magnetic field lines [47]. On a magnetic surface, turbulent eddies have two velocity components, one parallel to the magnetic field $V_{\parallel}$ and the other perpendicular to the magnetic field $V_{\perp}$. The elliptical model [48, 49] which takes into account the decay of turbulence eddies, is applied to

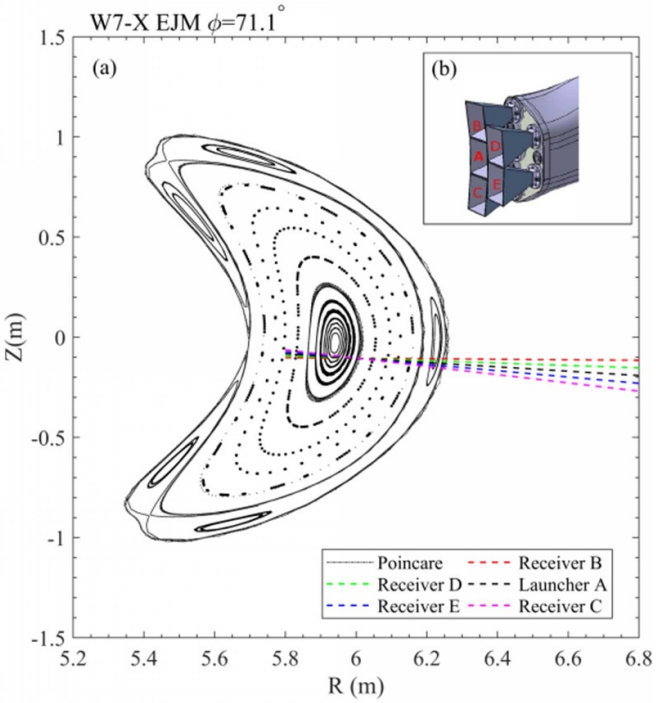

Figure 1. PCR's antenna arrangement and their LoS in standard magnetic configuration in W7-X. (a) The Poincaré map and the LoS of PCR antennae, (b) the antennae arrangement.

calculate the perpendicular velocity measured by PCR in W7-X [35, 50]. According to the elliptic model $V_{\perp}$ is expressed as:

$$V_{\perp} = \Delta s \Delta t / \left(\tau_0^2 + \Delta t^2\right), \tag{1}$$

where (Δt) is the delay time calculated via the cross correlation function (CCF), it stands for the time delay of a turbulent structure propagating between antenna combinations with the separation of (Δs). τ_0 is the time corresponding to the intersection point where the auto correlation function (ACF) is equal to the maximum amplitude of CCF. And it represents the time when the turbulence pattern decays when propagating between space-arranged detectors. It is generally known that the perpendicular velocity measured by PCR is the composition of both the plasma $E \times B$ velocity and the phase velocity of the density fluctuations: $V_{\perp} = v_{E\times B} + v_{\mathrm{phase}}$. Under the assumption that $V_{E\times B} \gg v_{\mathrm{phase}}$, the perpendicular velocity is thought to be $V_{E\times B}$. The v_{phase} of turbulence [42] on W7-X was estimated by comparing the measurements from a triple Langmuir probe and PCR. A small v_{phase} ($<0.4\ \mathrm{km\,s^{-1}}$) was obtained compared with the $V_{\perp}$ ($>6\ \mathrm{km\,s^{-1}}$). Therefore, the assumption of $V_{E\times B} \gg v_{\mathrm{phase}}$ is justified.

The coherence analysis is used to identify the similarity between two time series signals $x(t)$, $y(t)$. The coefficient γ is defined as

$$\gamma = \frac{|P_{xy}(f)|}{\sqrt{|P_{xx}(f)||P_{yy}(f)|}}, \tag{2}$$

where $P_{xy}(f)$ and $P_{xx}(f)$ or $P_{yy}(f)$ denote the cross-power spectral density (CPSD) and auto-power spectral density (APSD), respectively. Moreover, the integrated power spectra density ((IPSD) power is integrated over the frequency range of interest ([23], figure 10)) is usually used to calculate the amplitude of the turbulence.

3. Experimental results

In section 3.1, the LFM is characterized in the EJM configuration by PCR and Mirnov Coils [51] and in section 3.2 the turbulence modulation and velocity oscillation caused by LFM are investigated. Furthermore, the influence of the control coil current on the LFM is studied in detail in section 3.3.

3.1. Characteristics of LFM

Figure 2 shows the time evolution of the program of #180919034, where the stored energy of plasma is around the value of 500 kJ. The plasma is sustained by electron cyclotron resonance heating (ECRH) with a power of about 4 MW and a radiated power of 0.8 MW and both are constant during the whole discharge, as can be seen in figure 2(*a*). Figure 2(*b*) shows the time traces of the line-integrated density which is kept at $n_e \approx 6 \times 10^{19}\mathrm{m}^{-2}$, figure 2(*c*) shows the toroidal plasma current which is ramping up to 5 kA till the end of the program. Figure 2(*d*) shows that the time evolution of H_α. H_α is usually sensitive to MHD events and the modulation on it is evidenced by the 1.2 kHz mode in spectrograms of figure 2(*e*). It is noted that H_α is mainly emitted by neutrals recycled from the wall when particle fluxes reach the plasma facing components, and a modulation in H_α is also a hint that the LFM modulates the radial particle transport. Moreover, the LFM can be seen in the spectrogram of all antenna receivers of PCR till the end of the discharge at a constant frequency. Shown in figure 2(*f*) is the low frequency part of the cross-power spectrum from antenna combination BD and the sweeping frequency scans of PCR. As introduced in section 2, the sweeping of the frequency for each scan corresponds to different radial positions. The LFM is observed for the whole scan, which means the LFM covers the full radial range which is accessible for the PCR.

A coherence analysis is carried out between PCR and Mirnov coils in order to confirm the electromagnetic features of the LFM. Figures 3(*a*)–(*c*) show the APSD of antenna C from PCR, the APSD of one Mirnov coil and the coherence between the two signals. It is seen in figure 3(*b*) that the LFM is observed as a magnetic fluctuation at constant frequency and amplitude throughout the discharge. A clear coherence between PCR and the Mirnov coils is observed in figure 3(*c*), indicating the electromagnetic nature of the LFM.

By mapping the measurement of PCR from time domain to major radius R, the radial localization of LFM can be obtained. Figure 4 shows the results from the scan of 3.7 s–4.4 s. In figure 4(*a*) the Poincaré map of flux surfaces and the

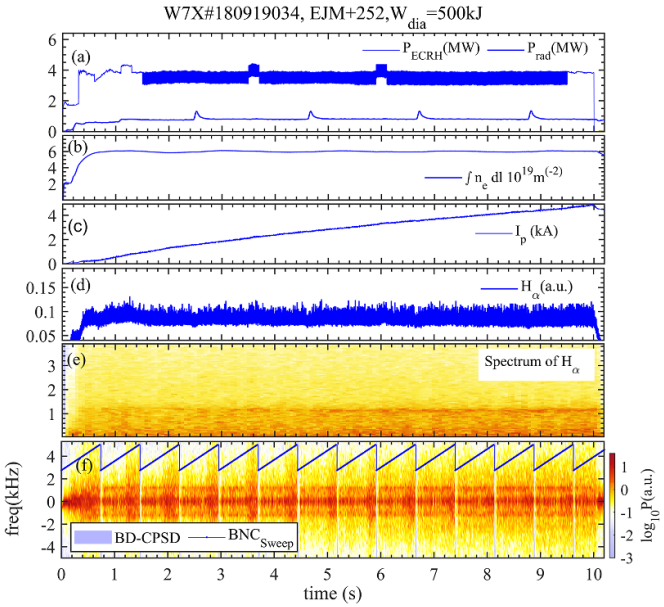

Figure 2. Plasma in EJM configuration for #180919034 showing the time evolution of (*a*) the ECRH power (P_{ECRH}) and the radiation power (P_{rad}), (*b*) the line-integrated density $n_e \approx 6 \times 10^{19}\mathrm{m}^{-2}$, (*c*) the plasma current (I_p), (*d*)–(*e*) the H_α emission signal and its spectrum, (*f*) the low frequency part of the cross-power spectrum of combination BD and the sweeping frequency of PCR.

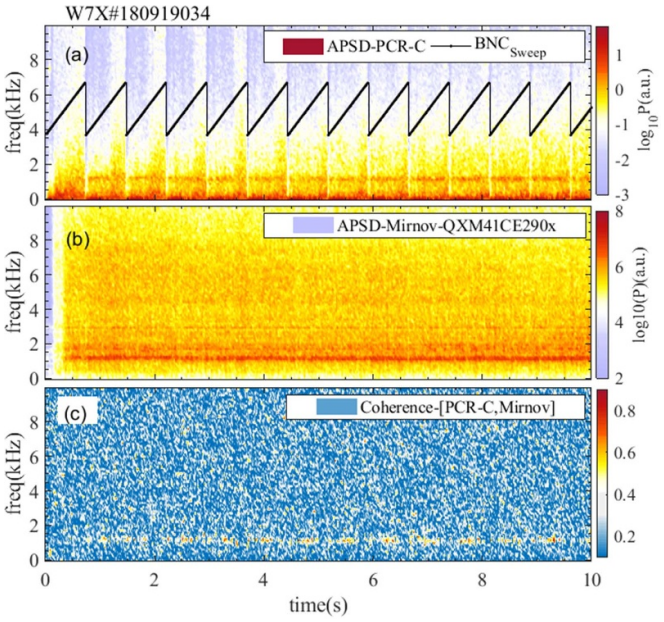

Figure 3. Coherence analysis between PCR and Mirnov coils. (*a*) and (*b*) are APSD of antenna C and the sweeping frequency of PCR and APSD of magnetic fluctuation from Mirnov coils, (*c*) coherence between those two quantities.

color coded connection are shown. For the calculation of the Poincaré map and the connection length, not only the main coils which generate the vacuum field but also the iota corrected coil are taken into consideration. Furthermore, the effect of plasma current (I_p) is taken into account by adding the mean plasma current obtained in the scan interval as an additional

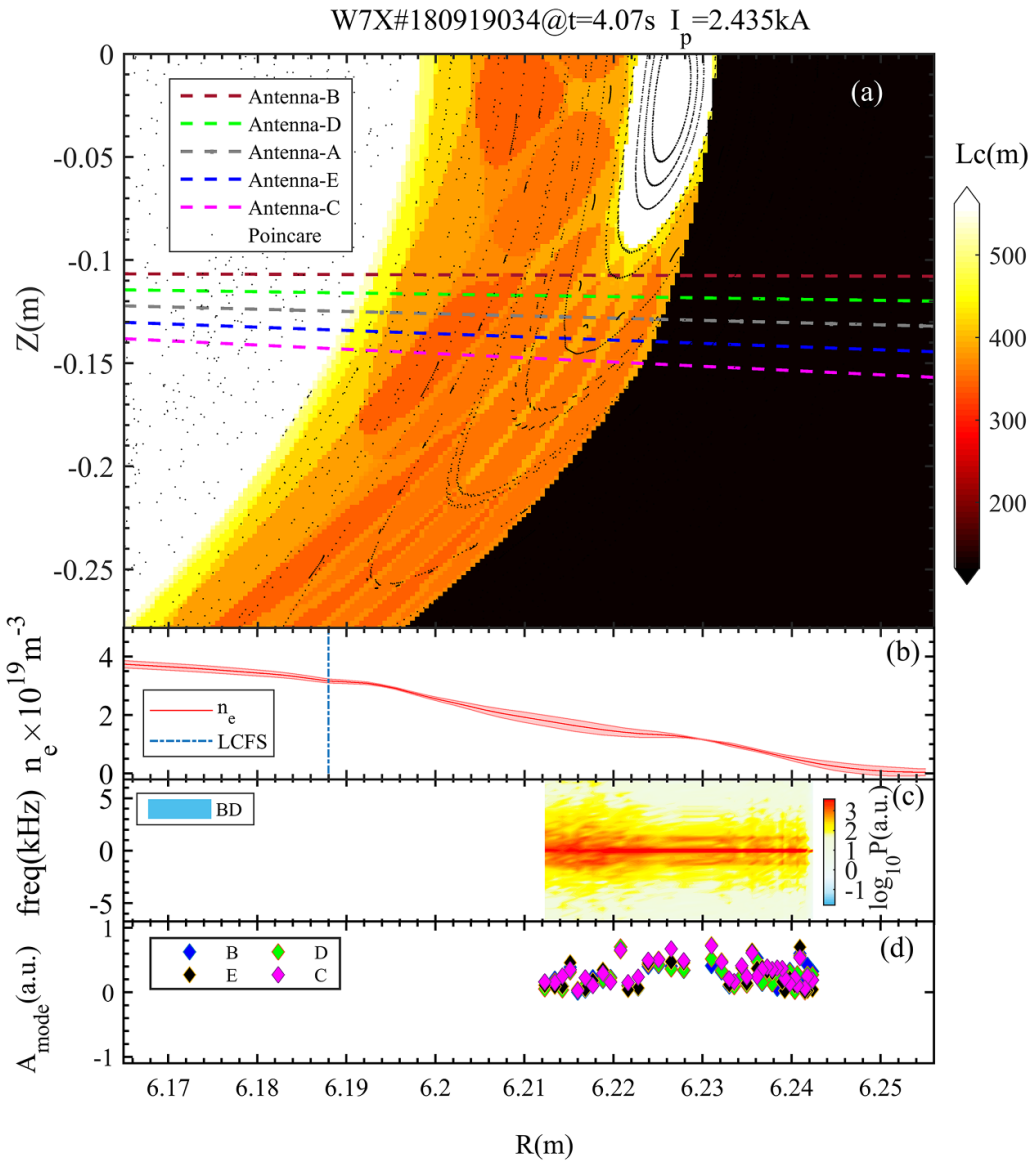

Figure 4. The radial distribution of LFM. (*a*) The Poincaré map indicated by the grey dots, the connection length is shown in color, the LoS of PCR antennae is shown as straight dashed lines in different color, (*b*) the density profile, (*c*) CPSD of antennae combination BD and (*d*) the amplitude of LFM for the four antennae.

current at the magnetic axis. The divertor plates are not shown here and are also not taken into account when calculating the Poincaré map. Ideally, the whole island structure will be kept when there is no intersection with the divertor plates. As soon as the magnetic island intersects with the divertor, the field lines close to the separatrix of the island are cut open and the connection length is no longer infinite. Only at the core of the magnetic island, it is still not perturbed by the divertor, and the connection length of field lines is infinite. This region is called remnant island. Figure 4(*a*) shows that the remnant island exists at 6.22 m $\leqslant R \leqslant$ 6.23 m, the region $R \geqslant$ 6.23 m is far-SOL, and outside the LCFS, the region $R \leqslant$ 6.22 m is the near-SOL. Considering the poloidal extension of the remnant island, it is noted that the LoS of antenna B is in the SOL and 1 cm–2 cm below the X-point of remnant island. Figure 4(*b*) shows the mapped density profile obtained from ABES, and the LCFS estimated for the LoS of PCR launcher (indicated by vertical dashed line, obtained from the field line tracer) at 6.188 m. The radial localization of PCR measurement is obtained according to this density profile, as seen in figures 4(*c*) and (*d*). It is found that all the measurements of the PCR are outside the LCFS, as seen in figure 4(*c*). Even in this case (as seen in figures 10 and 11) the measurement of PCR passes across the LCFS, and the LFM is seen in the SOL, only. Therefore, LFM is a mode localized in SOL. Furthermore, the LFM shows nearly constant frequency within the radial region of measurement. A closer look at the amplitude distribution of the LFM can be seen in figure 4(*d*). The amplitude of the LFM is extracted from its peak above the background in APSD, that is $P_{\mathrm{mode}} - P_{\mathrm{background}}$. It is seen

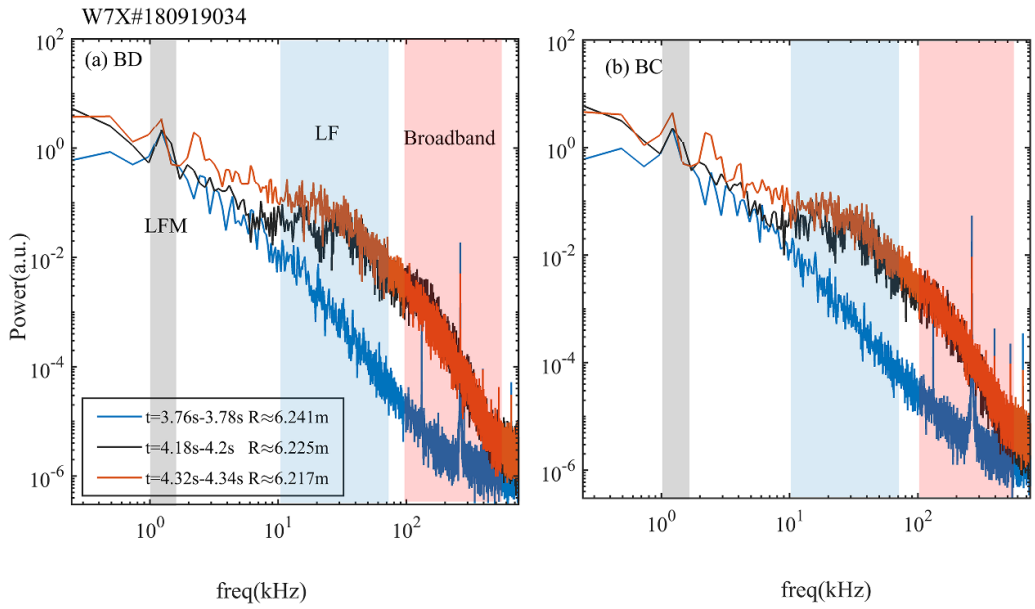

Figure 5. The CPSD for antennae combinations BD (*a*) and BC (*b*) for three different radial positions (blue curve is $R \approx 6.241$ m, black curve is $R \approx 6.225$ m, orange curve is $R \approx 6.217$ m). The shaded areas of grey denotes the LFM, the blue one the low frequency turbulence (LF, 10 kHz–80 kHz) and the red one the broadband turbulence (BB, 100 kHz–500 kHz), respectively.

that the amplitude of the LFM is almost constant outside the LCFS.

3.2. Modulation of turbulence by LFM

Turbulence properties are of large interest because they play a key role in the cross-field transport in the SOL, especially in the island divertor at W7-X. A closer look at the different turbulence components is shown in figure 5. Figures 5(*a*) and (*b*) show the CPSD analysis of antennae combinations BD (shortest poloidal separation) and BC (largest poloidal separation) at three different radial positions, e.g. $R \approx 6.217$ m, $R \approx 6.225$ m and $R \approx 6.241$ m, respectively. Both spectra are calculated for a time interval of 20 ms. It is seen that the antennae combinations BD and BC show similar spectral features. The LFM at a frequency of 1.2 kHz is clearly seen in all spectra for both combinations. Comparing the spectra at three different radial positions shows that the turbulence in the frequency range of 10 kHz–500 kHz is enhanced strongly for $R \approx 6.225$ m and $R \approx 6.217$ m. The power of the turbulence component at 100 kHz–500 kHz decays faster than that one of 10 kHz–80 kHz, which is seen from different slopes in the spectra. In order to verify whether the LFM has a modulation effect on the ambient turbulence, the turbulence spectrum ($f \geqslant 10$ kHz) is divided into different parts according to the power decay, (i) low frequency component (LF, 10 kHz–80 kHz, shaded in blue) and (ii) the broadband turbulence (BB, 100 kHz–500 kHz, shaded in red) for $R \approx 6.225$ m and $R \approx 6.217$ m. For $R \approx 6.241$ m, there is no change in the power decay, therefore, a component of 10 kHz–500 kHz is taken. Shown in figure 6 are the spectra of the IPSD within the frequency limits distinguished above for the three different radial regions for the combinations BD and BC. The time trace of turbulence amplitude for a specific component is obtained by calculating the IPSD. The modulation effect of LFM on different turbulence components is distinguishable from the analysis of the time trace of IPSD. The solid line presents the spectra of the IPSD LF and the dashed line presents the BB part. It is noted that in all spectra in figure 6, a clear peak at the frequency of the LFM is observed, indicating that both the BB-turbulence and LF turbulence are modulated by the LFM. It is interesting to note that the peak-power of LFM in the LF turbulence is much more pronounced than the LFM frequency in BB turbulence, revealing that the LFM imposes a more significant modulation effect on LF turbulence than on the BB turbulence.

In addition, evidence for the modulation effect of the LFM on turbulence can be found in the analysis of the Mirnov coils. In order to extract the fluctuation amplitude, the power of the turbulence component of 10 kHz–500 kHz is integrated. Figure 7(*a*) shows the time trace of the IPSD calculation, and a pronounced oscillation in the IPSD is visible around 1.2 kHz. In order to illustrate the 1.2 kHz is LFM, the cross-correlation is carried out between the IPSD from PCR of antenna B and IPSD of Mirnov coils in the frequency range of 10 kHz–500 kHz, as shown in figures 7(*b*) and (*c*), the CPSD and the squared coherence. A peak at an LFM frequency dominates both spectra, indicating that the modulation of density fluctuations and magnetic fluctuations are strongly correlated, both caused by the LFM.

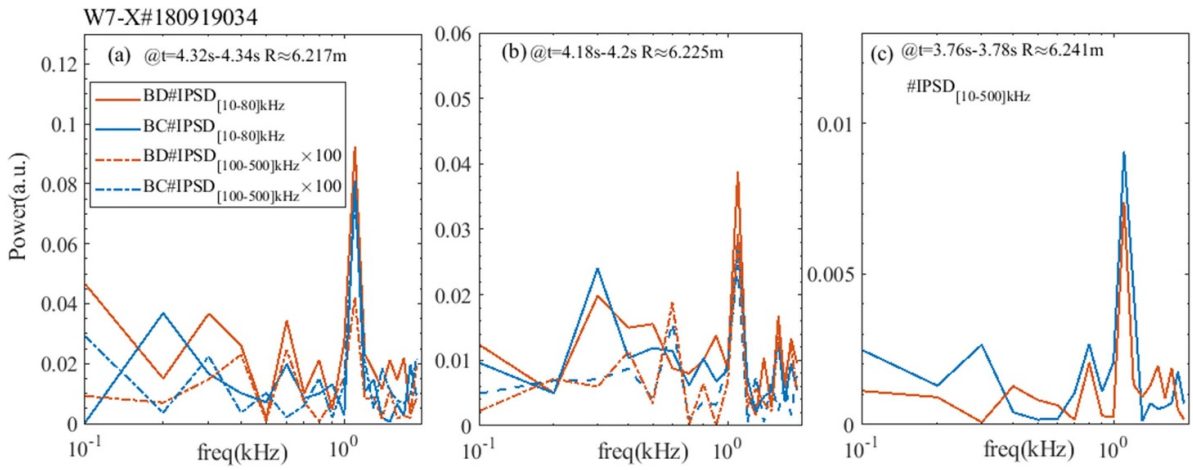

Figure 6. The spectra of integrated power spectra density (IPSD) of density fluctuation measured by PCR in orange of combination BD and in blue of combination BC. For solid line indicates IPSD at LF (10 kHz–80 kHz) and dash-dot line of BB (100 kHz–500 kHz) in (*a*) of $R \approx 6.217$ m and (*b*) of $R \approx 6.225$ m and of $R \approx 6.241$ m, 10 kHz–500 kHz in (*c*), respectively.

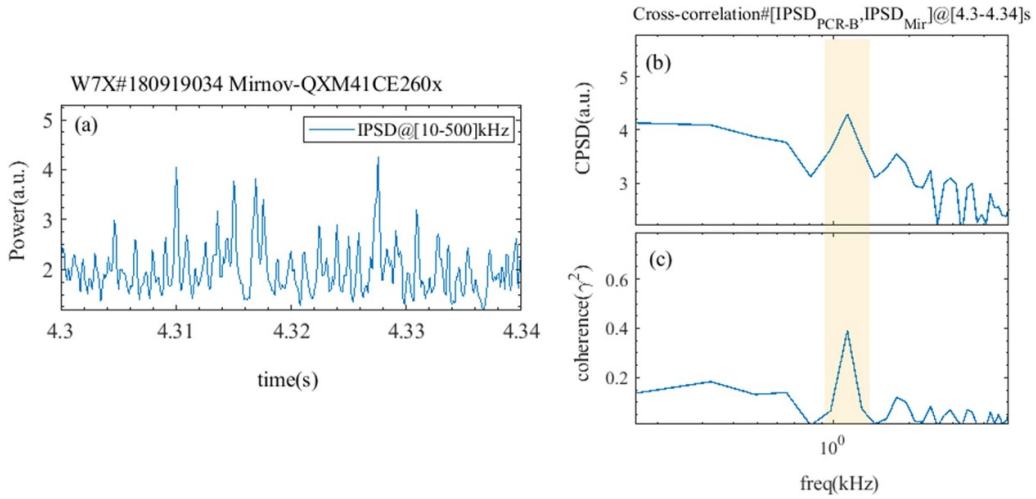

Figure 7. The coherence analysis between IPSD from PCR and Mirnov coils at the fluctuation components at 10 kHz–500 kHz, (*a*) time evolution of IPSD for magnetic fluctuation, (*b*) is the CPSD and the (*c*) is the squared coherence.

3.3. Modulation of perpendicular velocity by LFM

As seen from equation 1, the perpendicular velocity is calculated according to two determined delays. One is τ_0 from the elliptical model and the other is Δt. It is of interest to study the possible oscillation of these delays, and thus the modulation of $V_\perp$. The study is carried out on the ACF and the CCF as mentioned in section 2. In order to exclude the influence of the LFM, a band-pass filter of 10 kHz–500 kHz is applied to the raw signal. Then, due to the high sampling rate of PCR (4 MHz), the time window for the time delay calculation is carried out on 250 μs, result in a 4 kHz sampling rate. Since the mean period of the LFM is around the 1.2 kHz, it is possible to resolve the possible oscillations at the LFM frequency. Figure 8 shows the results of calculations for different quantities averaged over antennae combinations except for BD in the time window of 4.28 s–4.36 s. Figure 8(*a*) shows the time trace of the width of ACF ($\overline{\sigma_{\rm ACF}}$), which indicates the averaged turbulence auto-correlation time and figure 8(*b*) is the time trace of the averaged time-delay ($\overline{\Delta \rm t}$). Figure 8(*c*) is the time trace of the averaged time of $\overline{\tau_0}$, and figures 8(*d*) and (*e*) show the time trace of the averaged perpendicular velocity and perpendicular correlation length. Figures 8(*f*)–(*j*) show the spectra obtained from the signal in each panel, respectively. It is seen that the oscillation in $\overline{\sigma_{\rm ACF}}$ is more pronounced than the one in $\overline{\Delta \rm t}$, thus a pronounced peak in the spectra of figure 8(*f*) than that in figure 8(*g*). A similar observation is seen between $\overline{\tau_0}$ and $\overline{\Delta \rm t}$ as well. The oscillation is more pronounced in $\overline{\tau_0}$ (figure 8(*h*)) than that in $\overline{\Delta \rm t}$ (figure 8(*g*)). Furthermore, a clear oscillation on the $V_\perp$ is seen in figure 8(*d*), according to the results shown here, and equation 1, the main contributor, is the oscillation of τ_0. The oscillation of perpendicular velocity is around 1.09 km s^{-1}, corresponding to a ratio of normalized standard deviation

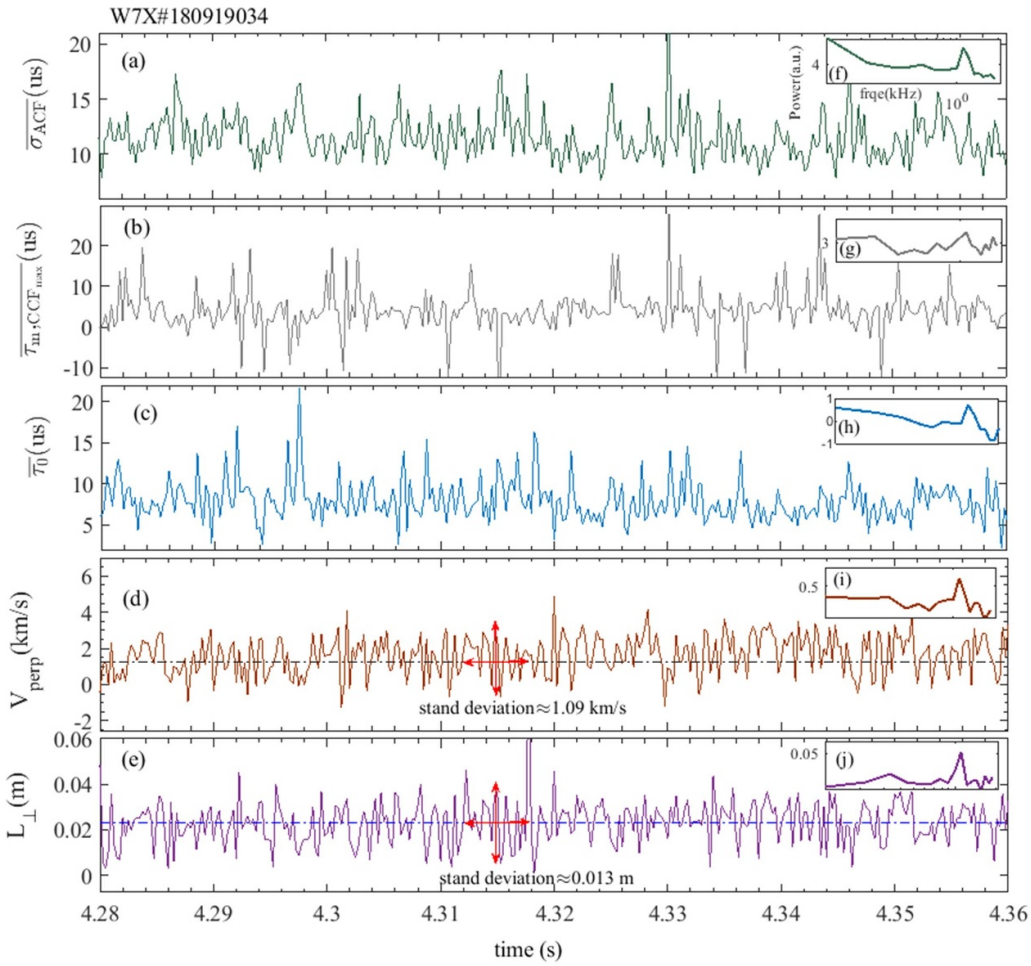

Figure 8. Time evolution of different quantities averaged for antennae combinations expect BD with time resolution of 250 ms in the window of 4.28 s–4.36 s, (*a*) is the averaged $\overline{\sigma_{ACF}}$ donates the turbulence auto-correlation time, and (*b*) is the averaged time delay ($\overline{\Delta t}$), (*c*) is the averaged mapped time delay of $\overline{\tau_0}$, (*d*) and (*e*) show the perpendicular velocity and perpendicular correlation length. Black dashed dotted line in (*d*) presents the mean value of perpendicular velocity of 1.25 km s^{-1} and the blue dashed dotted line in (*e*) presents the mean value of perpendicular correlation length of 2.3 cm. (*h*)–(*j*) are the spectra obtained from the signal shown in each panel, respectively.

divided by the mean value of ≈87%. Taking into account the ion sound speed($C_s = ((T_e + T_i)/m_i)^2$ and assuming $T_e \approx T_i \approx 30$eV, the oscillation amounts to ≈3.3%. The oscillation in velocity is further seen by a single peak of 1.2 kHz in the spectra of figure 8(*i*). The perpendicular correlation length of the turbulence eddy is described as $L_\perp \approx V_\perp \times \sigma_{ACF}$. Without the oscillation, the mean value of $L_\perp$ is 2.3 cm, and ±1.3 cm is induced by the LFM. This is seen also in the spectra of the correlation length (see figure 8(*j*)), meaning that the turbulence eddy size is modulated periodically.

3.4. Cross correlation between perpendicular velocity oscillation and turbulence modulation

As presented above, the perpendicular flow and characteristics of turbulence, e.g. ACF, IPSD and perpendicular correlation lengths are all modulated by the LFM. It is of interest to study the correlations between the turbulence modulation and velocity oscillations. Figure 9 shows the coherence analysis between them within the time window of 4.3 s–4.4 s. For the IPSD shown here, the integration range covers the frequency range of 10 kHz–500 kHz. Figures 9(*a*) and (*c*) show the CPSD, coherence and cross phase between perpendicular velocity and the IPSD for antennae combinations EC and BE. There is a pronounced peak in the CPSD and coherence indicating that the velocity oscillations and turbulence modulation are strongly correlated with each other. A very preliminary analysis of the cross phase, shown in figure 9(*c*), shows nearly no phase difference. This sheds some light on the fact that the LFM is not a zonal flow observed broadly in other devices since a phase difference [52, 53] is expected between E_r oscillation and turbulence amplitude modulation. However, the interpretation of this measurement is out of the scope of the paper.

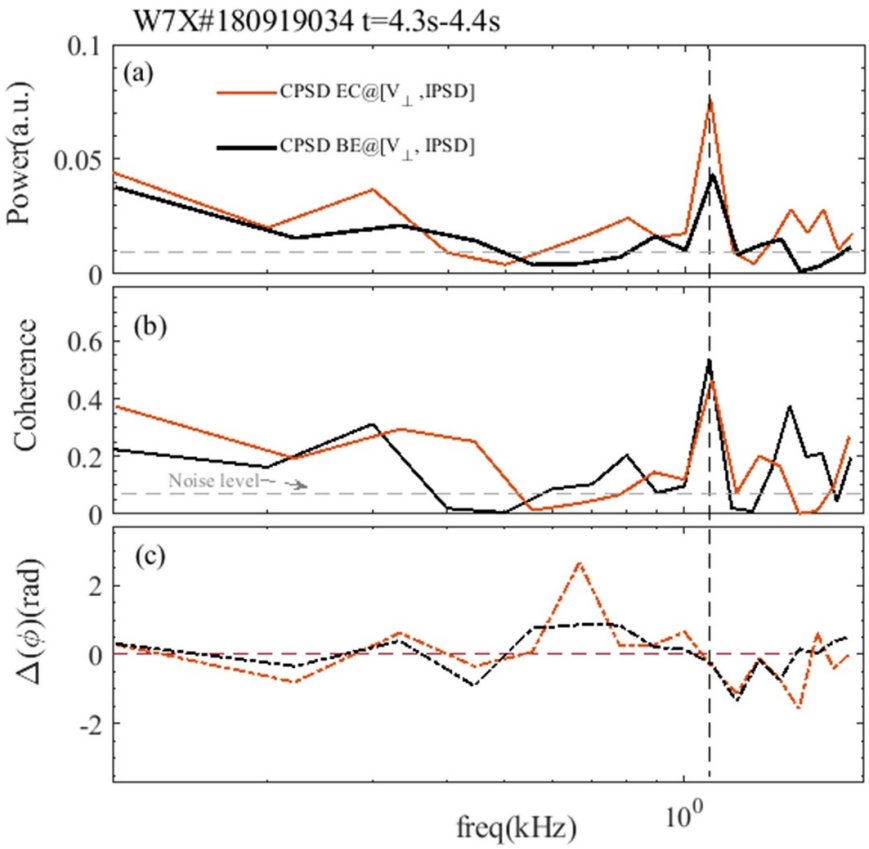

Figure 9. Coherence analysis. With (*a*)–(*c*) indicate the CPSD, coherence and cross phase between the perpendicular velocity and the IPSD for the antennae combinations EC and BE. The vertical dashed line in each figure indicates the LFM.

3.5. Evolution of LFM during the control coils currents scan

As introduced in 2, the divertor control coils (I_{cc}) are capable of modifying the shape and position of the divertor islands, which causes a significant modification of the magnetic topology at the plasma edge and the SOL. Previous studies have shown that the behavior of (I_{cc}) could influence the heat load on the divertor targets [54], the turbulent structures, like Quasi Coherent Mode (QCM) [41] and the edge plasma rotation [35]. Here, the influence of different I_{cc} on LFM is presented.

The effect of control coils on the LFM is studied by a comparison of three programs of #180816011/#012/#013, with similar plasma parameters but different I_{cc} as shown in figure 10. The plasma is sustained by ECRH with a power of 3.3 MW, as seen in figure 10(*a*). The diamagnetic energy of the plasma is ≈300 kJ and the plasma current ramps up similarly and saturate at ≈8 kA till the end of the program. Figure 10(*b*) shows the time trace of the control coil current, which is applied after 6 s with the absolute current ramp rate of ($|\mathrm{d}I_{cc}/\mathrm{d}t| = 150\mathrm{As}^{-1}$). In the program #180816011 the control coil current is positive I_{cc}, while for the program #180816012, the control coil current is negative. For the program #180816013, alternating control coil current has been set. It is noted that the line integrated density of these three programs is at a medium level of $3.5 \times 10^{19}\mathrm{m}^{-2}$, therefore a part of PCR measurements for each scan is localized inside the LCFS. The time delay at the plasma edge is always negative, wherein the SOL the time delay is positive [35], as indicated in figure 10(*c*). Furthermore, the evolution of the time delay for those scans, where the control coil currents are ramped shows a different behavior. Those differences are mainly due to the magnetic topology modification at the plasma edge and SOL. Figures 10(*d*)–(*g*) show the Poincaré maps and connection length in the poloidal cross section of the PCR for two different time slices, e.g. $t = 3.61$ s without the control coils shown in figure 10(*d*), and $t = 10.27$ s, with the absolute value of control coil current of 0.615 kA, for figures 10(*e*)–(*g*), respectively. As introduced in section 2, the increase in plasma current will change the edge iota therefore the position of the island varies. A consequence of this shift is a change in the size of the remnant island as well as a change in the intersection with the divertor plates. In general, an increase in the remnant island size goes along with an increase in the plasma current. The application of a positive control coil current will increase the size of the remnant island further. And application of negative control coils current the island size shrinks compared to the case without control coil current.

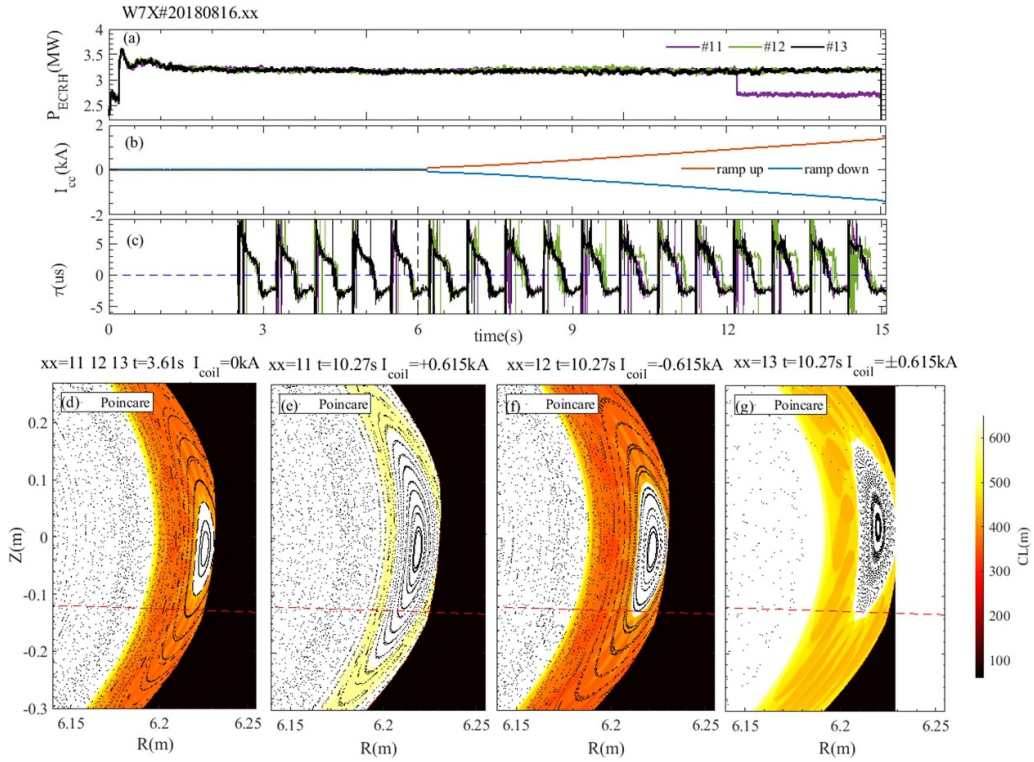

Figure 10. Plasma conditions for application of different control coil currents. Time traces of (*a*) P_{ECRH}, (*b*) the control coil current, with red line indicates control coil current ramps up and blue line indicates control coil current ramps down. (*c*) Time delay obtained by BE antenna combination, the black dashed line indicates control coil currents on at $t = 6$ s, (*d*)–(*g*) Poincaré map and connection length at cross-section of PCR at two different time slice, e.g. $t = 3.61$ s without the control coils shown in (*d*), and $t = 10.27$ s, with absolute value of control coil current of 0.615 kA, with #180816011 in (*e*), #180816012 in (*f*) and #180816013 in (*g*), respectively. Red dashed line indicates the LoS of PCR launcher.

Moreover, the application of the alternating powering of control coil currents will shift the island position poloidally. In figure 10(*f*), an increase in island size (island size influenced by both the plasma current and control coils) is observed when compared with that in figure 10(*d*). Comparing figure 10(*e*) with figure 10(*d*), it can be clearly seen that in figure 10(*e*) the LoS intersects the remnant island, and the radial distance of SOL along the LoS of PCR decreases. Furthermore, the connection length in SOL increases, too. Comparing figures 10(*d*) and (*g*), both the connection length and remnant island size are increased. Moreover, the LoS of PCR is close to the X-point of remnant island. Given these strong topology changes in the SOL, it is of interest to study their impact on the LFM.

The behavior of the LFM for different I_{cc} can be clearly seen in figures 11(*a*)–(*c*). Before the onset of the I_{cc} at 6 s, all the three programs showed no LFM activity. For the program #011, shown in figure 11(*a*) with positive I_{cc} ramp up, no LFM is observed for the whole discharge. Furthermore, other edge diagnostics of the LoS going across the SOL are also not seen in the LFM, which is consistent with the PCR observations. While for program #012, shown in figure 11(*b*) where a negative I_{cc} ramp is applied, the LFM appears at $t \approx 7.04$ s with the frequency of 1.25 kHz which increases to 1.75 kHz (points marked in diamond) until $t \approx 8.26$ s. Afterward the frequency decreases again to 1.25 kHz and at $t \approx 13.2$ s, it disappears. For the program #013 with the $\pm I_{cc}$, the LFM starts to appear at $t \approx 7.8$ s with a frequency of 1.75 kHz which is constant till the end of the program. Figure 11(*d*) shows the frequency scans of PCR after applying the I_{cc}. A staircase of frequencies with a duration of 20 ms for each step is denoted by the grey dots. The measurements in the time interval of 200 ms is marked by a black line, corresponding to a positive time delay for each sweep as shown in figure 10(*c*). During this time interval the LFM is observed and it is used for the calculation of the amplitude. The LFM amplitude evolution is shown in figure 11(*e*). The LFM amplitude is extracted according to the method introduced in 3.1. Figure 11(*e*) shows the time traces of LFM amplitude, it is seen that for program #011, no LFM is observed and therefore the LFM amplitude is close to noise level. For program #012, the LFM appears around $t \approx 7$ s and increasing the amplitude, sooner after $t \approx 9$ s the amplitude decreases gradually and finally disappear after $t \approx 13$ s. And for program #013, the LFM continuously increases the amplitude after it appears till around $t \approx 14$ s, and finally saturated. From the analysis above, it is found that LFM is observed in the cases when the LoS of PCR is close to the X-point of remnant island.

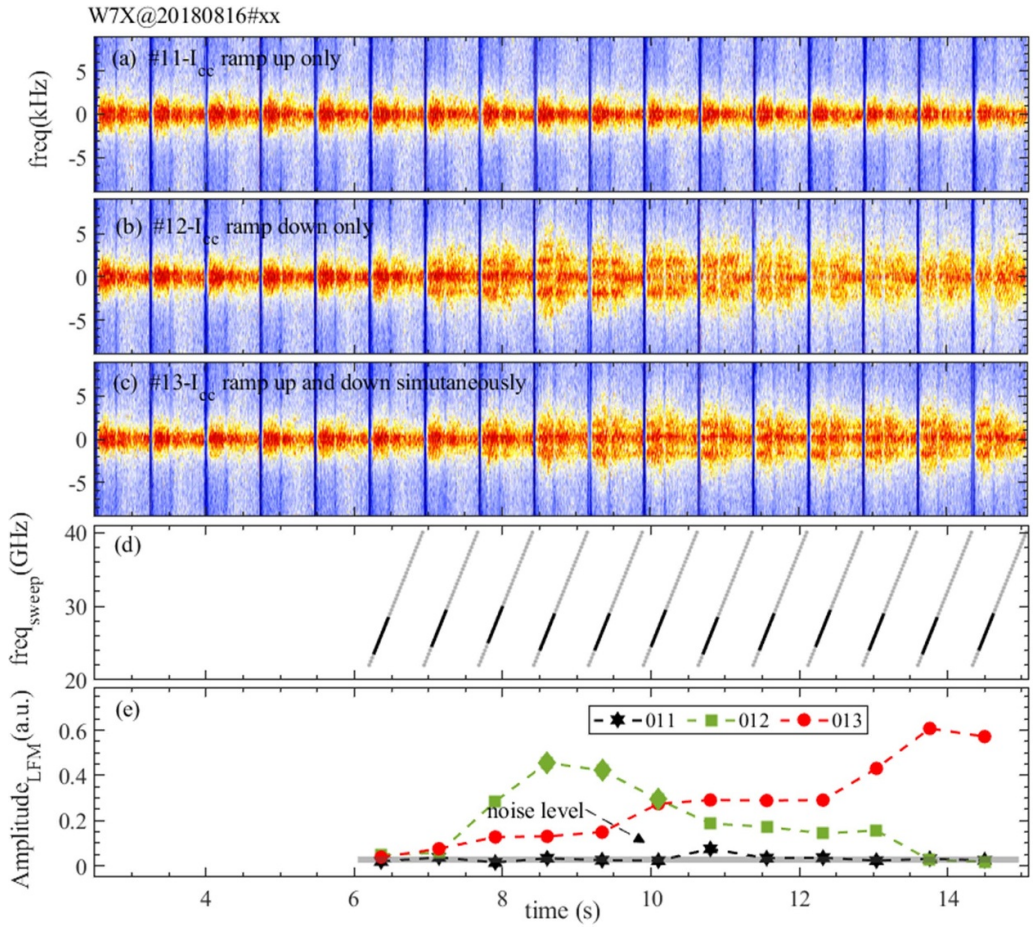

Figure 11. LFM evolution before and after applying the control coil. (*a*)–(*c*) are low frequency part of APSD from antenna B, with #180816011 in (*a*), #180816012 in (*b*) and #180816013 in (*c*), respectively. (*d*) Time traces of PCR sweeping frequency, with grey dots indicate different sweep and on top of each scan the black dots indicate the frequency steps selected for calculate the LFM amplitude. (*e*) Presents the LFM amplitude extracted according to the method introduced in 3.1 after applying the control coil for three programs. The points marked in diamond indicate the timing where the frequency is 1.75 kHz for #180816012.

To investigate a possible non-linear interaction and energy transfer among various turbulence components, a bi-coherence analysis is applied [55]. The bi-coherence is defined as:

$$b^2(f_1,f_2) = \frac{|<X(f_1)X(f_2)X^*(f3)>|^2}{<|X(f_1)X(f_2)|^2><|X(f3)|^2>}, \qquad (3)$$

where $X(f)$ denotes the Fourier transform of the signal X, with $X^*(f)$ being the complex conjugate of $X(f)$. And the angular brackets refer to the ensemble average. The value of $b^2(f_1,f_2)$ is bounded between 0 and 1, which describes the strength of nonlinear coupling between three phase coherency waves satisfied with $f_3 = f_1 + f_2$. The corresponding summed bi-coherence, defined as $b^2_{\text{sum}} = \frac{1}{N(f)}\sum_{f=f_1+f_2} b^2(f1,f2)$ and $N(f)$ is the number of Fourier components for each f in the summation. Contour plots of the bi-coherence spectrum and its summed spectra, calculated from the magnetic signal in two different time windows, are compared in figure 12. Before application of control coils (no LFM is observed), the bi-coherence spectrum of figure 12(*a*) shows nearly no coupling among different components. After the presence of the control coils (LFM appears), significant of bi-coherence is observed at LFM frequency $(f_1 + f_2 = f_{\text{LFM}}, f_2 = \pm f_{\text{LFM}})$ in figure 12(*b*) and in the summed bi-coherence (figure 12(*c*)). The strongly coupling around f_{LFM} suggests a non-linear interaction or energy transfer between LFM and background turbulence. Therefore, a possible mechanism is that the nonlinear coupling of turbulence components is responsible for the LFM generation.

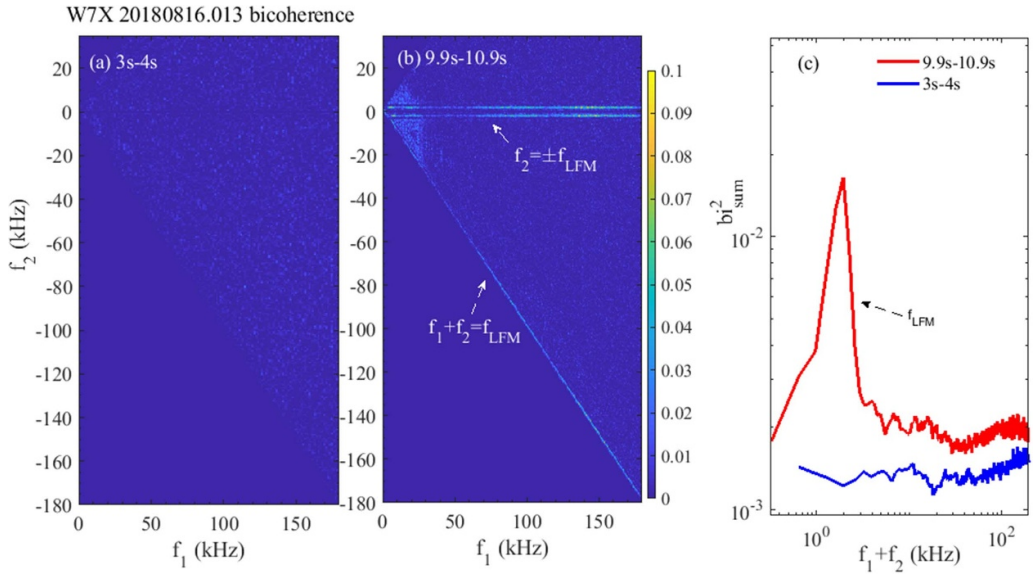

Figure 12. Bi-coherence analysis of magnetic fluctuation before (*a*) and after (*b*) applying the control coil for #180816013, and (*c*) the corresponding summed bi-coherence.

4. Discussion and summary

This work presents the study of a low frequency mode (LFM) in the standard magnetic configuration. The LFM appears in a large fraction of island divertor experiments in W7-X for the campaign of OP1.2b. From the measurements of a PCR, for the first time, the radial localization of LFM and its influence on the plasma turbulence and plasma flow are studied. The LFM is a coherent oscillation with a peak frequency varying in the range of $1-2$ kHz, $\Delta f \approx 200$ Hz. It is localized in the SOL region and its frequency is constant and its amplitude shows small variations radially. The electromagnetic characteristics have been realized by a cross correlation analysis with the Mirnov coils. Furthermore, the magnetic fluctuations and density fluctuations in the frequency range of $f \geqslant f_{\mathrm{LFM}}$ are modulated by this LFM. The perpendicular flow calculated by the elliptical model shows a clear oscillation at the LFM frequency. According to this elliptical model, τ_0 is the main contributor to the plasma flow($V_\perp$) oscillation. Moreover, the perpendicular correlation length of the turbulence eddy is also modulated by the LFM. A strong coherence between the turbulence modulation and velocity oscillations is observed. And a close to zero cross phase is obtained. The measured phase difference is different from the expected phase difference in the case of a zonal flow shown in other devices. The modification of the magnetic topology at the plasma edge by the application of external control coils allows to adjust the island size and position. It is observed that the appearance, frequency and amplitude of this low frequency mode is affected by the application of different control coil currents. During the experiments with control coils, the LFM is observed in the cases when the LoS of PCR is close to the X-point of the remnant island. Bi-coherence analysis shows that a nonlinear coupling of background turbulence is responsible for the generation of LFM.

However, some open questions still remain which are beyond the scope of the paper. The control coils in W7-X play a key role in adjusting the island divertor, which is of importance to exhaust the particles and heat flux. The influence of the LFM on the particle flux is confirmed by the modulation of the H_α signal, as shown in figure 2. The observed behavior of LFM during the application of control coils is of large interest and more important since SOL transport is not only influenced by the LFM but also overlapped with the effects imposed by the control coils on the magnetic topology. Further investigation of the dynamics of the LFM and its influence on the SOL transport, heat and particle flux distributions in the divertor are necessary. Due to the lack of edge profile measurements in OP1.2b, the investigation of the aforementioned issues is impossible. Another important factor is that a better mapping method is required between different diagnostics because of the intrinsic 3D structure of SOL in W7-X.

Acknowledgments

This work has been carried out within the framework of the EUROfusion Consortium, funded by the European Union via the Euratom Research and Training Programme (Grant Agreement No. 101052200 EUROfusion). Views and opinions expressed are however those of the author(s) only and do not necessarily reflect those of the European Union or the European Commission. Neither the European Union nor the European Commission can be held responsible for them. And this work was supported by the National Natural Science Foundation of China under Grant (Nos. 11605235, 12175277, 11975271, 12075155, and the National Key R&D Program of China (Nos. 2022YFE03050003, 2022YFE03070004) as well.

ORCID iDs

H.M. Xiang https://orcid.org/0000-0001-7799-6190
A. Krämer-Flecken https://orcid.org/0000-0003-4146-5085
X. Han https://orcid.org/0000-0001-8498-6433
G. Weir https://orcid.org/0000-0002-2370-409X
K. Rahbarnia https://orcid.org/0000-0002-5550-1801
J. Schilling https://orcid.org/0000-0002-6363-6554
A. Knieps https://orcid.org/0000-0003-0083-7188
M. Vécsei https://orcid.org/0000-0003-4596-1211
S. Zoletnik https://orcid.org/0000-0002-7324-2647
D. Zhang https://orcid.org/0000-0002-5800-4907
T. Zhang https://orcid.org/0000-0002-1555-6226
X. Gao https://orcid.org/0000-0003-1885-2538
Y. Liang https://orcid.org/0000-0002-9483-6911

References

[1] Conway G. 2008 *Plasma Phys. Control. Fusion* **50** 124026
[2] Garbet X. *et al* 2004 *Plasma Phys. Control. Fusion* **46** B557
[3] Gusakov E. *et al* 2013 *Plasma Phys. Control. Fusion* **55** 124034
[4] Doyle E. *et al* 2007 *Nucl. Fusion* **47** S18
[5] Jenko F., Dorland W., Kotschenreuther M. and Rogers B. 2000 *Phys. Plasmas* **7** 1904–10
[6] Ren Y. *et al* 2017 *Nucl. Fusion* **57** 072002
[7] Bardóczi L., Rhodes T.L., Carter T.A., La Haye R.J., Bañón Navarro A. and McKee G.R. 2017 *Phys. Plasmas* **24** 062503
[8] Guttenfelder W., Candy J., Kaye S., Nevins W., Bell R., Hammett G., LeBlanc B. and Yuh H. 2012 *Phys. Plasmas* **19** 022506
[9] Kikuchi M. and Azumi M. 2012 *Rev. Mod. Phys.* **84** 1807
[10] Biglari H., Diamond P. and Terry P. 1990 *Phys. Fluids* B **2** 1–4
[11] Yan Z., McKee G., Fonck R., Gohil P., Groebner R. and Osborne T. 2014 *Phys. Rev. Lett.* **112** 125002
[12] Tynan G., Cziegler I., Diamond P., Malkov M., Hubbard A., Hughes J., Terry J. and Irby J. 2016 *Plasma Phys. Control. Fusion* **58** 044003
[13] Krämer-Flecken A., Soldatov S., Koslowski H.R. and Zimmermann O. (TEXTOR Team) 2006 *Phys. Rev. Lett.* **97** 045006
[14] Manz P. *et al* 2015 *Nucl. Fusion* **55** 083004
[15] Conway G.D., Smolyakov A.I. and Ido T. 2022 *Nucl. Fusion* **62** 013001
[16] Sun P. *et al* 2018 *Plasma Phys. Control. Fusion* **60** 025019
[17] Jiang M. *et al* 2020 *Nucl. Fusion* **60** 066006
[18] Bardóczi L., Rhodes T., Carter T., Navarro A.B., Peebles W., Jenko F. and McKee G. 2016 *Phys. Rev. Lett.* **116** 215001
[19] Bardoczi L., Rhodes T.L., Bañón Navarro A., Sung C., Carter T.A., La Haye R.J., McKee G.R., Petty C.C., Chrystal C. and Jenko F. 2017 *Phys. Plasmas* **24** 056106
[20] Jiang M. *et al* 2019 *Nucl. Fusion* **59** 066019
[21] Chen W. *et al* 2017 *Nucl. Fusion* **57** 114003
[22] Zhang T. *et al* 2019 *Nucl. Fusion* **59** 056020
[23] Xiang H. *et al* 2019 *Nucl. Fusion* **59** 106037
[24] Boozer A.H. 2009 *Phys. Plasmas* **16** 058102
[25] Helander P. *et al* 2012 *Plasma Phys. Control. Fusion* **54** 124009
[26] Beidler C. *et al* 1990 *Fusion Technol.* **17** 148–68
[27] Wolf R. *et al* 2008 *Fusion Eng. Des.* **83** 990–6
[28] Klinger T. *et al* 2019 *Nucl. Fusion* **59** 112004
[29] Renner H., Boscary J., Greuner H., Grote H., Hoffmann F., Kisslinger J., Strumberger E. and Mendelevitch B. 2002 *Plasma Phys. Control. Fusion* **44** 1005
[30] Liu S. *et al* 2019 *Nucl. Fusion* **59** 066001
[31] Zoletnik S. *et al* 2019 *Plasma Phys. Control. Fusion* **62** 014017
[32] Griener M. *et al* 2020 *Nucl. Mater. Energy* **25** 100854
[33] Ballinger S. *et al* 2021 *Nucl. Mater. Energy* **27** 100967
[34] Bozhenkov S., Otte M., Biedermann C., Jakubowski M., Lazerson S.A., Sunn Pedersen T. and Wolf R.C. 2018 *Nucl. Fusion* **59** 026004
[35] Krämer-Flecken A. *et al* 2020 *Plasma Sci. Technol.* **22** 064004
[36] Vershkov V., Dreval V. and Soldatov S. 1999 *Rev. Sci. Instrum.* **70** 1700–9
[37] Xiang H. *et al* 2018 *Rev. Sci. Instrum.* **89** 10H103
[38] Krämer-Flecken A., Soldatov S., Vowinkel B. and Müller P. 2010 *Rev. Sci. Instrum.* **81** 113502
[39] Windisch T., Krämer-Flecken A., Velasco J.L., Könies A., Nührenberg C., Grulke O. and Klinger T. 2017 *Plasma Phys. Control. Fusion* **59** 105002
[40] Krämer-Flecken A. *et al* 2017 *Nucl. Fusion* **57** 066023
[41] Han X., Krämer-Flecken A., Windisch T., Hirsch M., Fuchert G., Geiger J., Grulke O., Liu S. and Rahbarnia K. 2019 *Nucl. Fusion* **60** 016011
[42] Krämer-Flecken A. *et al* 2019 *Plasma Phys. Control. Fusion* **61** 054003
[43] Liang Y. *et al* 2017 *Nucl. Fusion* **57** 066049
[44] Bozhenkov S.A., Geiger J., Grahl M., Kisslinger J., Werner A. and Wolf R.C. 2013 *Fusion Eng. Des.* **88** 2997–3006
[45] Lazerson S.A., Loizu J., Hirshman S. and Hudson S.R. 2016 *Phys. Plasmas* **23** 012507
[46] Zoletnik S. *et al* 2018 *Rev. Sci. Instrum.* **89** 10D107
[47] Prisiazhniuk D., Conway G.D., Krämer-Flecken A. and Stroth U. (the ASDEX Upgrade Team) 2018 *Plasma Phys. Control. Fusion* **60** 075003
[48] Briggs B., Phillips G. and Shinn D. 1950 *Proc. Phys. Soc.* B **63** 106
[49] He G., Jin G. and Yang Y. 2017 *Annu. Rev. Fluid Mech.* **49** 51–70
[50] Han X. *et al* 2021 *Nucl. Fusion* **61** 066029
[51] Rahbarnia K. *et al* 2020 *Plasma Phys. Control. Fusion* **63** 015005
[52] Xu Y. *et al* 2014 *Plasma Phys. Control. Fusion* **57** 014028
[53] Nishizawa T., Almagri A., Anderson J., Goodman W., Pueschel M., Nornberg M., Ohshima S., Sarff J., Terry P. and Williams Z. 2019 *Phys. Rev. Lett.* **122** 105001
[54] Gao Y., Jakubowski M.W., Drewelow P., Pisano F., Puig Sitjes A., Niemann H., Ali A. and Cannas B. 2019 *Nucl. Fusion* **59** 066007
[55] Kim Y., Beall J., Powers E. and Miksad R. 1980 *Phys. Fluids* **23** 258–63